We are IntechOpen, the world's leading publisher of Open Access books
Built by scientists, for scientists

6,900
Open access books available

185,000
International authors and editors

200M
Downloads

154
Countries delivered to

Our authors are among the

TOP 1%
most cited scientists

12.2%
Contributors from top 500 universities

CLARIVATE ANALYTICS
BOOK CITATION INDEX
INDEXED

WEB OF SCIENCE™

Selection of our books indexed in the Book Citation Index
in Web of Science™ Core Collection (BKCI)

Interested in publishing with us?
Contact book.department@intechopen.com

Chapter

Testing and Validating Instruments for Feedstocks of Mineral Carbonation

Muhammad Imran Rashid

Abstract

Different feedstocks Dunite, Olivine and Lizardite are examined in this research using various measuring techniques such as TGA-MS, XRD and Quantitative XRD and EDS. Quantitative XRD results matched with TGA-MS results. Malvern Mastersizer, EDS and QXRD results also showed a good match regarding the individuality of results which are shown graphically. TGA-MS calibration curves example is provided. Matching the results of different measuring techniques is a key to fundamental research. Comparison of the reactivity of dunite, soaked dunite, heat-activated dunite and lizardite and raw dunite soaked has been performed. TGA-MS and QXRD results match each other. Malvern Mastersizer, EDS and QXRD results match with their individual results indicating the instrument's reliability. Semi-Quantitative XRD results authenticity is EXCELLENT. TGA-MS results match with QXRD is excellent. Mineral carbonation converts CO_2 into stable mineral carbonates. This research explores the utilisation of serpentinised dunite (which is comprised of 61% lizardite) as a potential feedstock for mineral carbonation. Heat activation, *ex-situ* regrinding and concurrent grinding techniques were employed to enhance the reaction rate and yield, and to provide information on the carbonation reaction mechanism. Silica-rich layers that appeared during reference experiments were disrupted using concurrent grinding and significantly higher magnesite yields and Mg extractions were obtained.

Keywords: CCS (carbon capture and storage), CCSU (carbon capture, storage and utilisation), mineral carbonation (MC), carbon capture (CC), materials science

1. Introduction

Greenhouse gases especially CO_2 concentration in the atmosphere has increased to a level of 419 ppm compared to a value of 280 ppm from the preindustrial revolution (1975) [1]. Reduction in greenhouse gases is a need of time. Significant research has been published regarding mineral carbonation [2–15], geological carbon dioxide storage, oceanic storage [3], carbon dioxide conversion into chemicals, carbon dioxide fixation in polymers and carbon dioxide conversion into Urea [16, 17]. Mineral carbonation is one of the forefront technologies recently proposed. Although various publications have been done in this field [2], the basic need of time is to foresee how

the research efforts need to be oriented or centred on that technology [3, 4, 9–11, 13, 14, 18–20]. This article will indicate some directions for the utilisation of different feedstocks for CO_2 utilisation and fixation. Geological storage poses a threat to nearby occupants as there were thousands of killings in the Crater Lake incident. ALOHA software can be used for the estimation of such leakages if CO_2 is to be stored in geological formations. CO_2 can cause asphyxiation; hence, safety measures are at most necessity. ALOHA can estimate CO_2 vapours travelling distances and how far this gas can travel and how much concentration will be at a specified point. Oceanic storage pose threat to aquatic life and is expected to disrupt the ecosystem seriously. Increased concentration of CO_2 in oceans [21] will reduce the pH of the oceanic water, rivers or canals making them undrinkable. Seawater is used in various industries. Reduced pH will cause serious corrosion issues and may result in materials damage and or stress corrosion cracking.

Greenhouse gases are uncontrollable. Each greenhouse gas concentration increases day by day. CO_2 is recently converted to jet fuel using sunlight by Adele Peters from Fast Company [22]. Researches are not giving up. However, the Antarctic lake has disappeared in just 3 days [23]. More efforts need to be initiated. Extremism in climate shattering weather patterns is expected right now [23]. Europe has seen extreme flooding in 2021. Pakistan has seen extreme summers like what the Middle East has seen shooting of temperatures. Catalysts have been discovered to convert CO_2 into fuel [24]. A single reason why CO_2 is not controlled is that industries emit more than capture. Adam Vughan has indicated that atmosphere warming could not have been kept below 1.5°C [25]. Alas, more seriousness is required. No negative emissions drama. The cement industry is also one of the largest CO_2 emitting industries. Novel modifications are proposed to overcome this threat [26]. Coal-burning emissions and their environmental effects are also highlighted [27].

2. Analytical instruments

Dunite, different varieties of olivine and lizardite are used in this research. Proper functioning of analytical instruments is a fundamental to perform the highest level of research. Fundamental instruments operation and working is described here.

2.1 TGA-MS analysis

Thermogravimetric analysis (TGA) measures the change in mass over time as the sample is heated. These measurements provide compositions of different feeds or carbonated products. TGA is suitable to characterise different materials that display mass loss or gain due to thermal decomposition and thus enable an estimate of magnesite yields of the carbonated products to be obtained. Feed materials or carbonated products were heated in TGA (**Figure 1**) from 25 to 1000°C and mass losses due to decomposition of different phases present are identified. To identify the evolving gases generated during heating, the TGA-DSC (Setsys Evolution 1200) was coupled with a mass spectrometer (Thermostar Quadrupole). The initial loss of mass observed between 25 and 280°C corresponds to physically bound moisture present in the sample, while the second mass loss from 280 to 430°C corresponds to brucite decomposition, while the third major mass loss in the range of 430–830°C corresponds to lizardite decomposition (**Figure 2**).
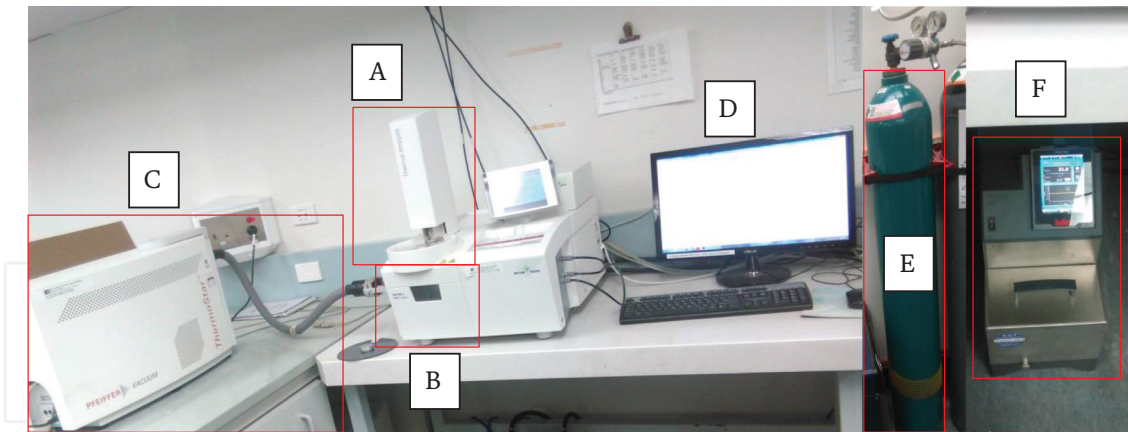
Figure 1.
Photo of TGA-MS set up. A, autosampler and small sample crucibles; B, TGA furnace where the sample is being heated; C, mass spectrometer connected with TGA furnace to receive evolved gases from TGA; D, computer for data output; E, argon cylinder for argon gas flow; F, chiller to cool down TGA furnace.
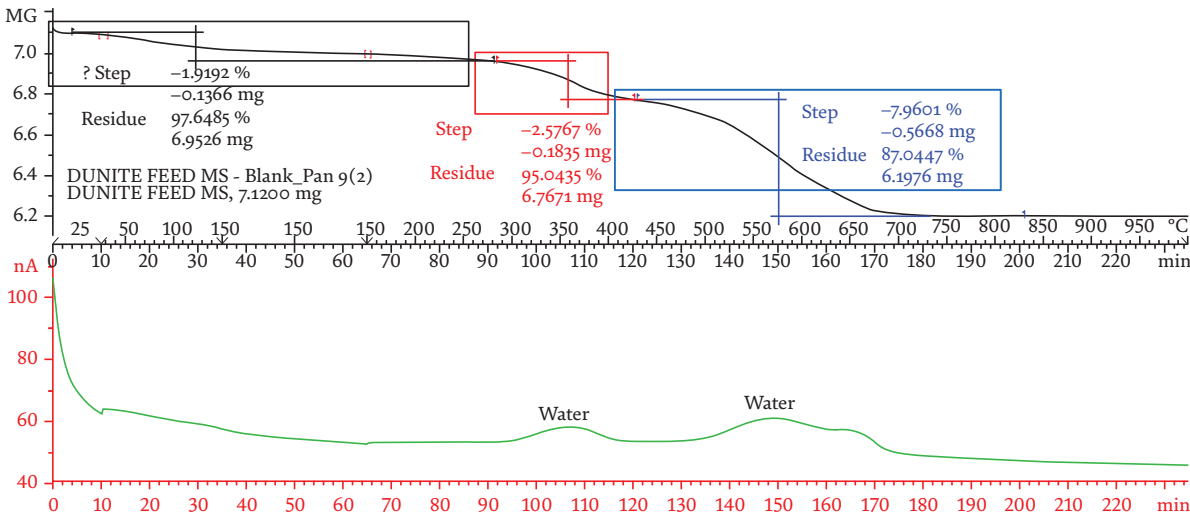

Figure 2.
Typical TGA-MS curve. The first significant loss of mass is due to moisture present in the sample. The second mass loss is due to brucite decomposition. The third mass loss is due to lizardite decomposition. All major changes in mass are due to the elimination of H_2O vapour from the sample.

Lizardite decomposes over the same temperature range (300–600°C) as the magnesite [6] and this can introduce a systematic error in magnesite yield estimation (leading to an over-estimation of the magnesite yield) unless the mass loss in this period can be quantitatively attributed to loss of H_2O or CO_2 from the sample. To distinguish between these species, the ion current from the m/z = 44 ion (CO_2^+) from mass spectrometer was calibrated using sodium bicarbonate samples and a calibration curve for CO_2 concentration was obtained, which is used to quantify CO_2 mass loss (distinguishing CO_2 production from the loss of water vapour, which occurs simultaneously) and thus render more accurate estimation of the magnesite yield. CO_2 peak areas were calculated using the mass spectrometer data and CO_2 mass response is estimated based on the reaction ($2NaHCO_3 \rightarrow Na_2CO_3 + CO_2 + H_2O$). The relationship between peak areas and CO_2 mass loss was linear.

For carbonated samples, the CO_2 peak areas were estimated using MS data and then these peak areas are used to determine CO_2 mass loss applying the CO_2

Step	Reaction [29]	Theoretical mass loss (%)	Measured mass loss (%)
1	$CaC_2O_4 \bullet H_2O \rightarrow CaC_2O_4 + H_2O$ (189°C)	12.3	12.6 ± 0.66
2	$CaC_2O_4 \rightarrow CaCO_3 + CO$ (502°C)	19.2	19.9 ± 0.98
3	$CaCO_3 \rightarrow CaO + CO_2$ (763°C)	30.1	31.2 ± 0.53

Table 1.
TGA calibration data for three runs.

calibration curve. This CO_2 mass loss was used in an equation to calculate magnesite yield. The equation is based on the Gadikota formula [28].

Three TGA runs (**Table 1**) were completed with calcium oxalate hydrate (99% pure) to calibrate the TGA response. Theoretical and measured mass loss shows good agreement (**Table 1**).

3. XRD analysis and QXRD (semi-quantitative XRD)

XRD analysis is useful in the determination of crystalline phases that exists in a powdered sample [30]. Each phase has a specific, identifiable x-ray diffraction pattern, which is used to determine different phases present in the sample. X-rays are generated from the emission of high energy electrons from hot tungsten elements, which are bombarded on a copper metal target. This bombardment causes an electron emission from target atoms, thus generating an electron vacancy which is filled by an electron from higher energy orbitals and this transition generates x-rays. Filtration of these x-rays is performed to get monochromatic radiation which is bombarded on the sample being analysed. Bragg's equation is the main law used in XRD diffraction pattern analysis [31].

$$n\lambda = 2d\sin\Theta \tag{1}$$

λ = wavelength of x-rays, n = integer, d = plane spacing, Θ = Bragg's diffraction angle.

To derive Bragg's law, consider two x-rays (A and D) impinging on the atom B and E of a crystal and the angle of incident and angle of reflectance are equal as shown in **Figure 3**. Incident waves A and D are in phase with each other although wave D has to travel an extra distance of GE + EH to remain in the same phase as wave A. This extra
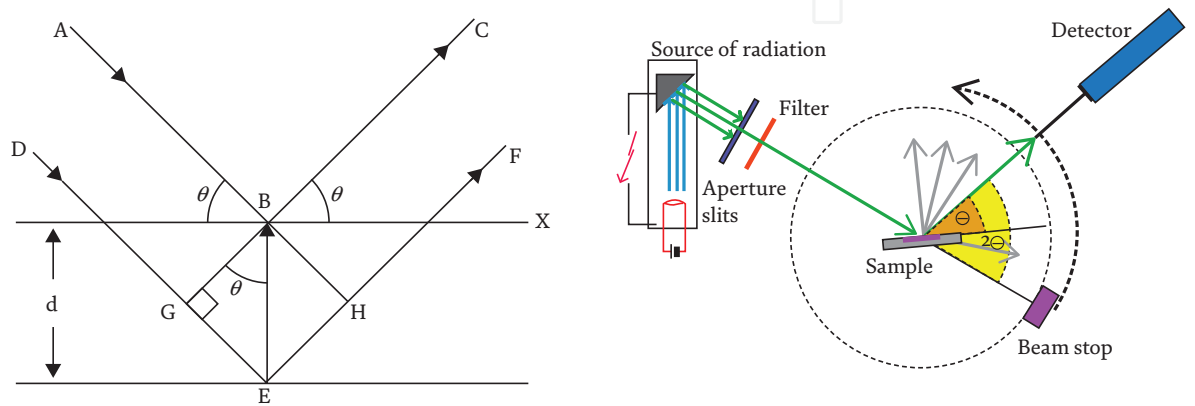

Figure 3.
Schematic of X-ray diffraction (left), Bragg–Brentano geometry (right).

distance must have been an integral (n) multiple of wavelength (λ). The length GE and EH are equal and GE equals to $d\ sinn\Theta$. Bragg–Brentano design is the most commonly used instrument geometry for high-resolution powder diffraction. The incident beam through a number of slits diverges towards the sample, the diffracted signal from the sample again converges through a number of slits towards the detector. A $\Theta/2\Theta$ rotation is employed to keep incident and diffracted wave paths in symmetry. During sample scanning, the sample rotates by Θ while the detector is rotated by 2Θ with each step [32].

In practice, finely ground feed materials and carbonated samples (up to 100 μm size particles) were put in the instrument holder for analysis. Samples were finely grounded in order to avoid intensity fluctuations and preferred orientation. XRD analyses were performed using Philips X'Pert Pro multipurpose diffractometer with Cu radiation and 2θ from 5 to 90° or 11 to 31° depending upon the sample being analysed. Collection time used was 1 s with a step size of 0.02°. The patterns from XRD were matched with the International Centre for Diffraction Data ® (ICCD) using X'Pert Highscore® in order to identify crystalline phases. A typical x-ray diffraction pattern for feed dunite is shown in **Figure 4**. Phases identified are lizardite, olivine, brucite and magnetite.

If the reference intensity ratio (RIR) of an analytical phase i (such as silicon) is known, then its concentration can be calculated by doping the original sample with the analytical phase. This can be done by the addition of a known amount of standard (silicon) of which the RIR is known. For semiquantitative method details please see below.

After obtaining the diffraction pattern of the doped sample, the concentration C_i in the original sample is calculated as follows:

$$C_i = A_x \times \left(\frac{I_i}{I_x}\right) \times \left(\frac{RIR_X}{RIR_i}\right) \qquad (2)$$

C_i = concentration of given phase i in the original sample
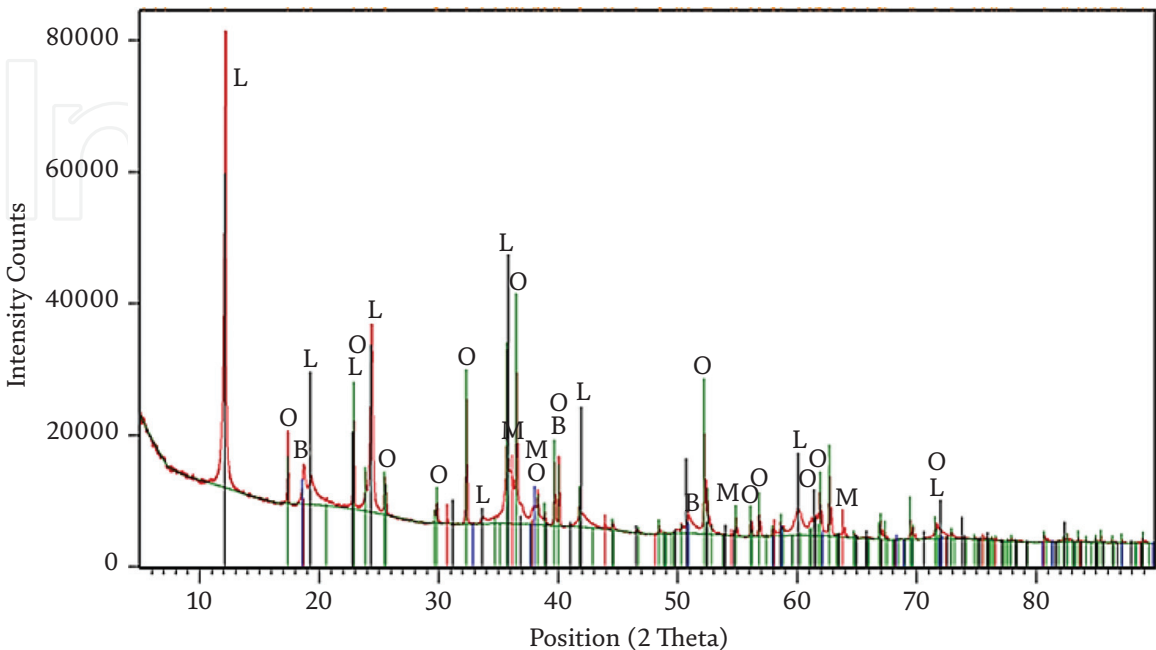Axe = known amount of standard (silicon) added to the original sample

Figure 4.
Typical x-ray diffraction pattern for dunite. L, Lizardite; O, olivine; B, Brucite; M, magnetite.

Position (2Θ)	Intensity			Formulas used
x	y	Y′	Area	
11.83	15,480	15,480	2.96	(Slope) $M = \frac{(y_2 - y_1)}{(x_2 - x_1)}$
11.84	15,924	15,468	11.0	(Intercept) $C = y - M \times X_1$
11.85	16,699	15,456	17.7	(Derivative) $Y' = M \times X_1 + C$
11.87	16,940	15,445	23.0	$Area = \frac{((y_1 - Y'_1) + (y_2 - Y'_2)) \times (X_2 - X_1)}{2}$
11.88	17,482	15,433	30.6	$C_i = A_x \times \left(\frac{I_i}{I_x}\right) \times \left(\frac{RIR_x}{RIR_i}\right)$ (3)
11.89	18,093	15,422	38.1	

Table 2.
Semiquantitative XRD analysis.

I_i, I_x = intensities (peak areas) of phases i and x in the doped sample
RIR_i, RIR_x = reference intensity ratio values of i and x respectively
The procedure is described below in detail (for calculation detail see **Table 2**)

1. Add known amount of silicon (usually 20 wt/wt%) in the sample and scan it with XRD

2. Identify phases present in a given XRD pattern

3. Determine the area under the main peak of each phase. The peak should not overlap other peaks. To calculate the area under the main peak, first, calculate slope (M) and then intercept (C). Then calculate derivative (Y′) and use the given formula to calculate the area under the peak (please refer to **Table 2**). Use these peak areas in Eq. (2).

4. The RIR value is found from the Highscore® database

5. The concentration C_i of each phase is estimated using Eq. (2)

3.1 ICP-OES (inductively coupled plasma: Optical emission spectrometry)

The elemental composition of solid and liquid samples can be determined using ICP-OES. ICP-OES consists of two major components; the torch and optical spectrometer. The torch comprises quartz tubes [33]. To produce plasma, argon gas is normally used, which passes through the tubes around the induction coil. The argon gas is "ignited" by the Telsa unit and the ionisation process (plasma formation) is initiated. The ionisation of argon gas occurs at this stage. A plasma having approximately 7000 K temperature is generated because of collisions between neutral argon atoms and charged particles [34]. Using a peristaltic pump, an aqueous sample is continuously supplied to the nebuliser where it changes to mist and moves to the plasma envelope. The introduced sample interacts with electrons and ions in the plasma and is converted into charged ions. This causes the decomposition of different molecules into respective atoms that lose electrons to induce the emission of radiation of distinctive wavelengths of elements present inside the sample. The optical spectrometer separates these wavelengths into component wavelengths. Intensities are
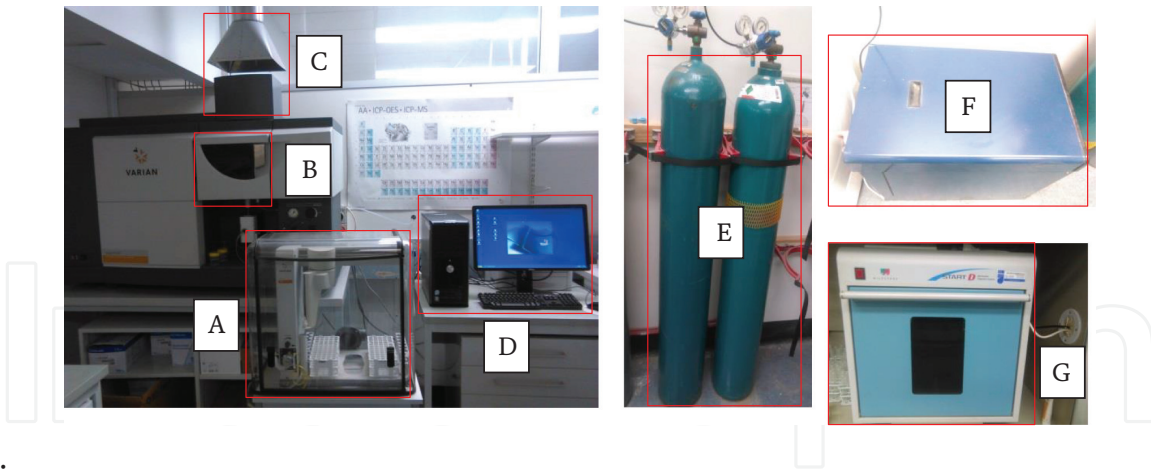
Figure 5.
Photo of the ICP-OES set-up and microwave digestion system. A, autosampler with standards and sample tube holders; B, plasma chamber; C, gases exhaust; D, computer for analysis output; E, argon gas cylinders; F, chiller; G, microwave digestion system.

compared with the intensities of standard solutions of known element compositions and elements concentrations are computed based on the calibration curves. ICP-OES set-up and microwave digestion system is shown in **Figure 5**.

Solid samples used in the present investigation were first digested in acidic solution. Dunite sample (0.1 g) was digested in a microwave oven (**Figure 5**) using a mixture of 4.5 mL HNO_3 (65%), 4.5 mL HCl (37%) and 3 mL HBF4 (tetrafluoroboric acid, 50%). Thulium (50 μL) was added as a tracking element. The volume of this mixture was increased to 20 mL by the addition of 2% nitric acid prior to its digestion in the microwave. Digestion was not required for supernatant solution samples and they are diluted using 2% nitric acid to the required level (50%/100% dilution) prior to their analysis by ICP-OES (Varian, Australia). The typical curve for ICP-OES is shown in **Figure 6**. Mg concentration drop with the passage of time due to magnesite precipitation. Si concentration increases during the first hour but then it stays constant, which is due to simultaneous silicon leaching from dunite and its precipitation in the form of silica.
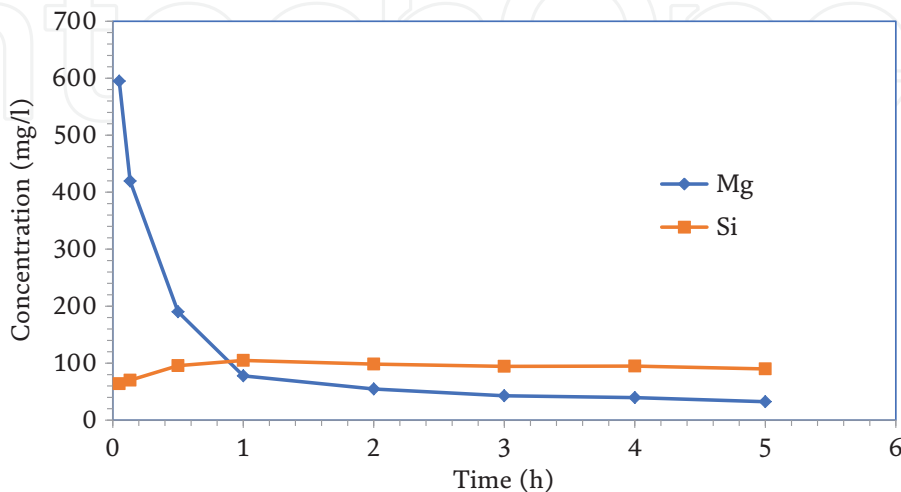

Figure 6.
Typical curve for ICP-OES. The graph represents Mg and Si concentrations variation with time for supernatant solution of sub 75 μm heat-activated dunite carbonated sample. Carbonation reaction was performed with 15% solids slurry at 185°C, 130 bar pressure and using 0.64 M $NaHCO_3$.

3.1.1 Scanning Electron microscope (SEM)/energy dispersive scattering (EDS)

Morphology, surface topography and elemental compositions of feed materials and carbonated products were determined using SEM (Zeiss Sigma VP FESEM) and EDS (Bruker). SEM scans a fine electron beam over the material being analysed and uses different detectors to reconstruct the image from signals produced from the sample [35]. SEM consists of different parts, e.g., microscope column which also includes electron gun and electron beam travels in this column; the computer that drives the microscope; ancillary equipment which analyses the composition. SEM can magnify objects from 10 times to 300,000 times. Scanning from an electron microscope can be compared with a person having a torch and looking for objects on the wall. As a person builds an image in his/her memory, SEM works in the same way and uses a fine electron beam instead of the torch to build an image.

EDS is a technique that provides information about the chemical composition of the sample. For EDS, an electron beam is focussed on the sample during SEM analysis and these electrons interact with the atoms. X-rays are produced from these interactions and an energy dispersive detector detects these x-rays and displays a signal in the form of spectrum, histogram or intensity versus x-ray energy. This makes it possible to identify elements present in the sample.

Sample preparation is important for SEM. Samples are gold (imaging) or carbon (EDS) coated prior to their analysis. Gold coating provides a thin layer to the samples and samples were coated four times at a 90° angle and fifth time from the top. A typical SEM micrograph and EDS spectrum of dunite feed sample are shown in **Figure 7**. SEM shows an image of the dunite feed and the EDS spectrum indicates intensities of the elements present in the sample. Polished resin blocks were used to study the silica-rich layers. Polished resin blocks were prepared using feed material, carbonated products and resin. Photo of polished resin blocks and sample holders is shown in **Figure 8**. The polished resin block samples preparation procedure is given in appendix 3D.

3.1.2 Transmission Electron microscope (TEM)

TEM is useful to study the structure, properties and compositions of different mineral powders, especially in the submicron range. Mineral particles should have
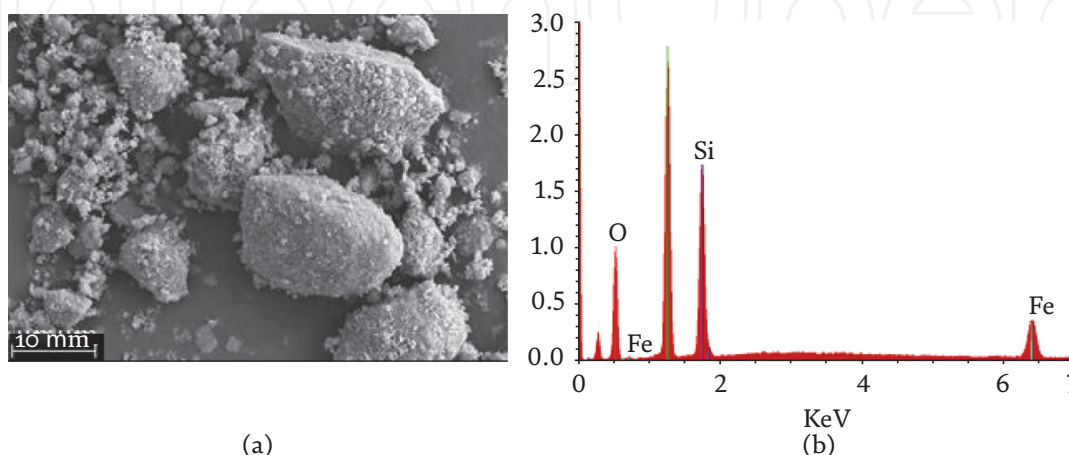

(a)   (b)

Figure 7.
SEM micrograph and EDS spectrum of dunite feed. (a) Dunite feed SEM micrograph, 10 μm is a resolution of the SEM (b) EDS spectrum of dunite feed, intensities of different elements are shown, Mg, magnesium; Si, silicon; O, oxygen; Fe, iron.

Figure 8.
Photo of the sample holders (left) and polished resin blocks (right).

been in 50–100 nanometres size to be properly analysed by TEM. Electrons transmission through the mineral particles enables detailed analysis of the particle features especially its crystal structure, orientation and chemical composition. In the present study, TEM was used to identify shell (silica-rich layers) and core part of the reacted mineral particles and study the corresponding elemental compositions and structure.

To prepare samples for TEM (JEOL 2100 TEM) analysis, 10 mg of sample powder was added to the pestle and mortar. Ethanol (4 ml) was mixed with the sample powder and contents were ground for 3 min. Ground sample was moved into a 5 ml plastic vile and sonicated for 20 min. Using pipette 1–2 drops were dropped on the TEM grid (200 mesh Cu, ProSciTech) and air-dried overnight prior to TEM analysis.

3.1.3 Fourier-transform infrared (FTIR) spectroscopy

FTIR is useful to acquire an infrared spectrum of a solid sample either feed or product. In FTIR spectroscopy, most molecules absorb light in the infra-red region of the electromagnetic spectrum and this absorption corresponds to the specific bonds present in the molecule. Measurement usually is in wave numbers typically over the range $4000–400 \text{ cm}^{-1}$. When the sample being analysed is exposed to radiation, some portion of the radiation is absorbed while other is transmitted. The block diagram of the FTIR spectrometer is shown in **Figure 9**. Dunite and carbonated products were analysed by FTIR (Bruker, Tensor 37 Spectrometer). Samples for FTIR spectroscopy were prepared using 99% KBr and 1% sample. Samples were thoroughly mixed and ground before making pellets. These pellets were placed in an oven under a vacuum at 150°C for 24 hours before analysis. Typical FTIR spectra of raw dunite are provided in **Figure 10**.

3.1.4 Malvern Mastersizer

Particle size distribution (PSD) of feed materials and carbonated products were determined using a particle size analyser (Mastersizer 2000, Malvern Instruments) (**Figure 11**). For particle size measurement, it is important how particles scatter and absorb light. Initially, the Fraunhofer model [36] was used to predict scattering patterns when a solid disc of particles is passed through the laser beam. This model failed to describe exact scattering as very few particles are disc-shaped. Mie theory is currently used which is able to predict the light scattering behaviour of all materials. Each size of particle has a specific scattering pattern. The particle size analyser uses the above-mentioned theories and works backwards to calculate particle
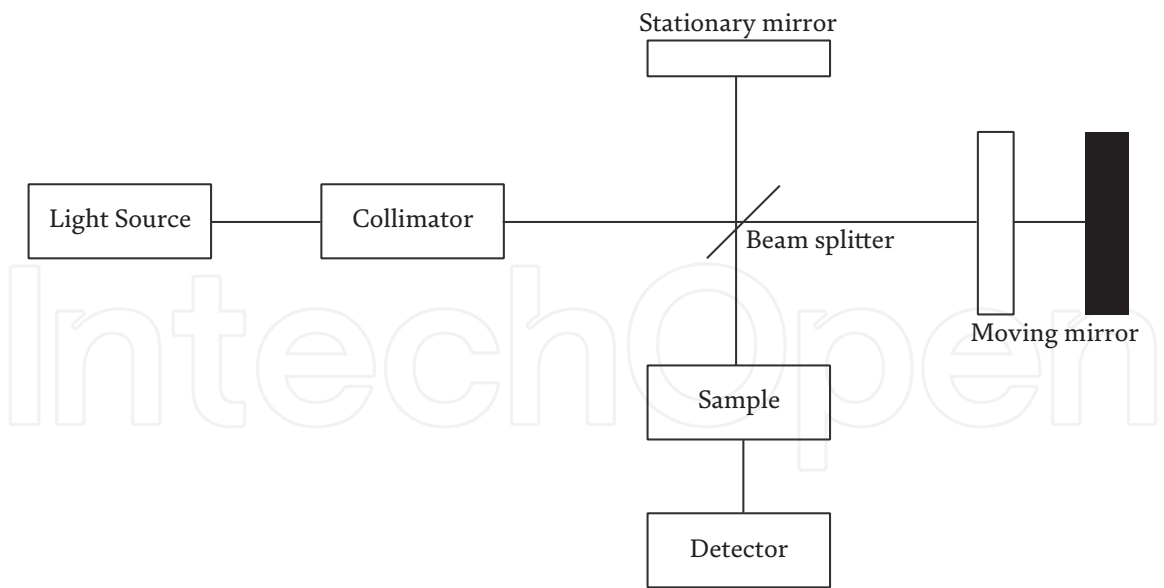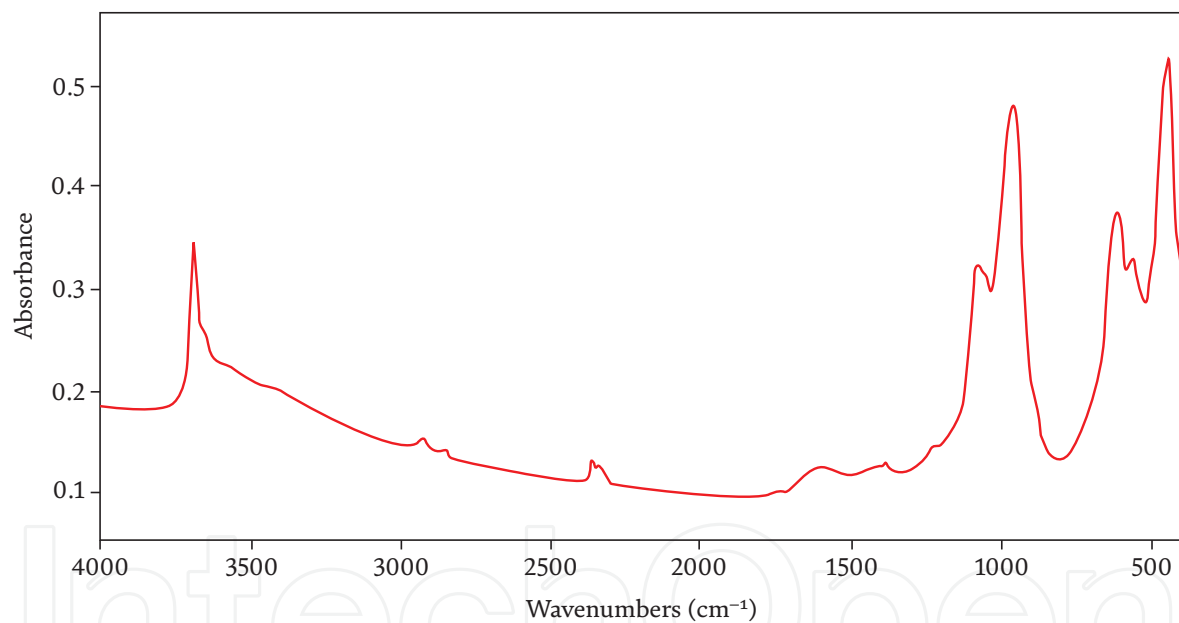
Figure 9.
Block diagram of FTIR spectrometer.

Figure 10.
Typical FTIR spectra of raw dunite, stretch present around 3690 cm^{-1} are due to presence of surface-bound OH moieties, the vibration at 1073 cm^{-1} due to out of plane vibration of Si-O, adsorption band at 970 cm^{-1} are in-plane Si-O stretching vibration, the feature at 629 cm^{-1} are due to deformation of hydroxyl groups, stretches at 564 cm^{-1} are Mg-O out of plane vibration, stretches at 450 cm^{-1} are Si-O-Si bond bending vibration (reference [9] and references therein).

size from the captured scattering pattern. Basic laser diffraction system is shown in **Figure 12**.

Three procedures are used for any particle size measurement. First, a sample is prepared and dispersed in a dispersion unit in proper concentration followed by its delivery to the optical bench. Second, a scattering pattern is captured from this sample which is also called "measurement" and is done by the optical bench. Third, raw data from measurement is analysed by instrument software to provide the PSD. Finely ground samples (≤20 μm) were preferably analysed in wet solution form. These samples tend to agglomerate during drying even if dried under vacuum and at low
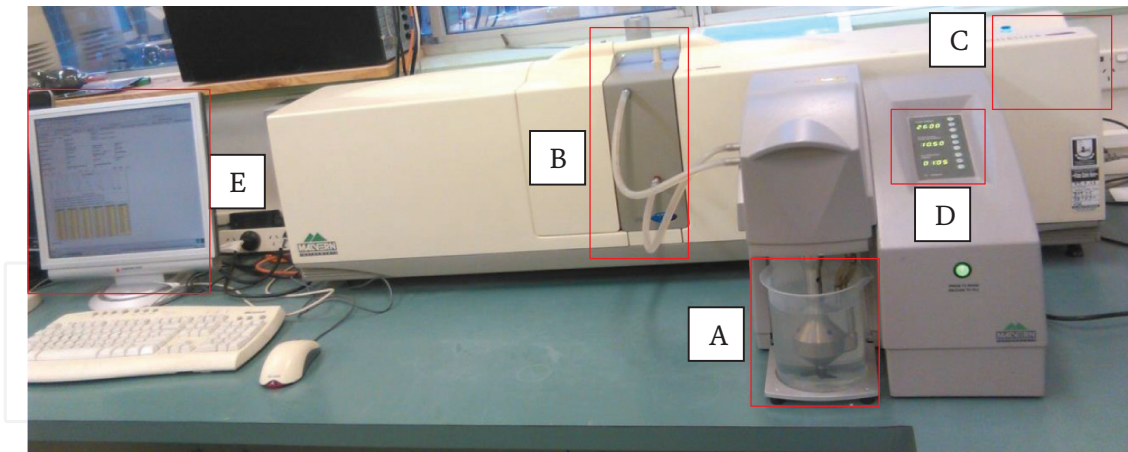
Figure 11.
Photo of Malvern mastersizer 2000. A: Sample dispersion unit and pump impeller, B: Sample cell where dispersed sample is moving and laser light pass through it, C: Laser source and laser ON indicator, D: Pump speed adjustment and ultrasound operation system, E: Computer to show output.
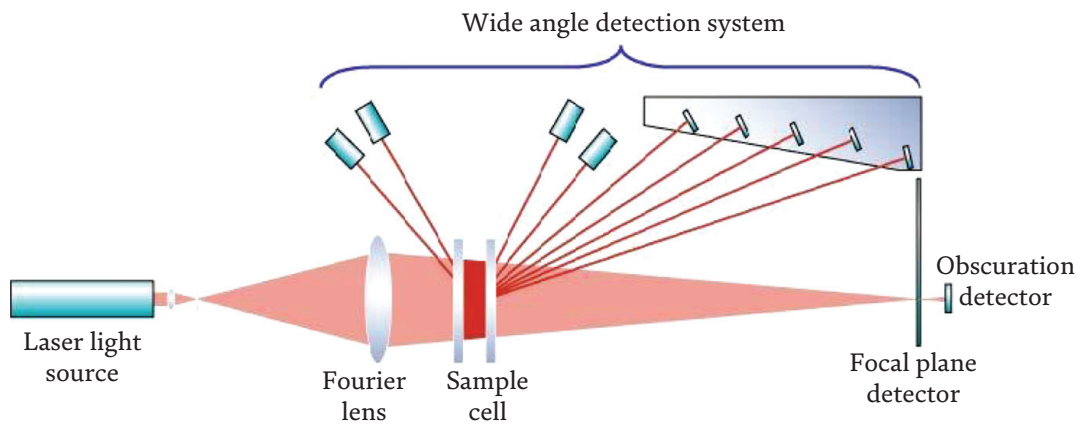

Figure 12.
Basic laser diffraction system of Mastersizer 2000.

temperatures (70°C). For these samples and heat-activated samples, a built-in ultrasonic system in the Malvern mastersizer was used to break any agglomerates present. A typical PSD from the Malvern mastersizer is shown in **Figure 13**. Size classes are represented on the x-axis in μm and the volume density of particles is represented in percentage on the y-axis. The percentiles, d_{10}, d_{50} and d_{90} are shown in **Table 3**. D_{10} means that 10% volume of particles is smaller than this size (27 μm), d_{50} means that 50% volume of particles is smaller than this size (42 μm) and d_{90} means that 90% volume of particles is smaller than this size (64 μm).

4. Results and discussion

Olivine (Netherland) and Olivine (Norway) characterisation using Quantitative XRD (X-Ray Diffraction) analysis is discussed. The supplier of these samples has promised to supply olivine; however, these appear as a mixture of olivine and a few other minerals. These samples may be rocks but still, Olivine (Norway) is probably like olivine as it has higher olivine content. This olivine content (62%) almost match lizardite content (61–62%) of the dunite [18] used primarily in my research.
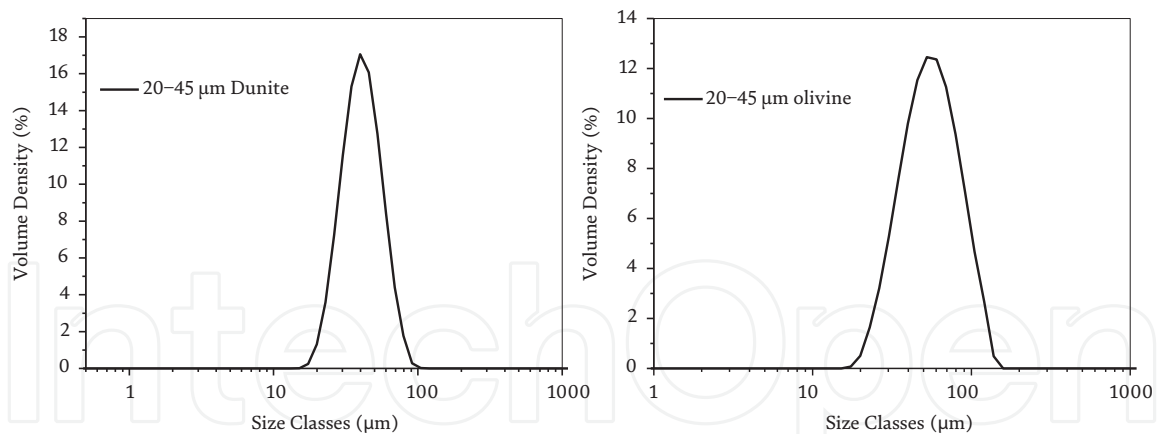
Figure 13.
PSD for 20–45 μm dunite (left), PSD for 20–45 μm olivine (right).

	d_{10} (μm)	d_{50} (μm)	d_{90} (μm)
20–45 μm dunite	27	42	64
20–45 μm olivine	26	45	76

Table 3.
PSD for 20–45 μm dunite and 20–45 μm olivine.

Component	Olivine (Norway) %	Olivine (Netherland) %
Olivine	62.01	8.40
Clinochlore	11.58	7.10
Lizardite	5.43	53.01
Orthopyroxene	9.993	Tremolite 21.73
Phlogophite+Annite	1.307	Dolomite + Pyroxene (8.15)
Halite	0.884	Magnesioferrite (1.15)
Chabazite-Ca	4.543	—
Cordierite	4.243	—
Total	100	100

Table 4.
Olivine (Norway) and olivine (Netherland) QXRD analysis.

Powders samples were prepared for QXRD analysis of olivine (Netherland) and olivine (Norway). **Table 4** shows the analysis. Please refer to earlier publications [2, 10, 13, 14, 18, 19] for detailed description of methods. TGA-MS curves are presented in **Figure 14**. TGA commonly used in mineral carbonation to obtain yields was coupled with MS (Mass Spectrometer). This enabled us to calculate yields for dunite rock as evolved CO_2 gas and water vapours were measurable. TGA-MS was routinely calibrated. One example of calibration curves is shown in **Figure 15**.

4.1 TGA-MS analysis of olivine (Norway) and olivine (Netherland)

Olivine (Norway) and Olivine (Netherland) were analysed using TGA coupled with MS (Mass Spectrometer). Results are presented in **Figure 14**.
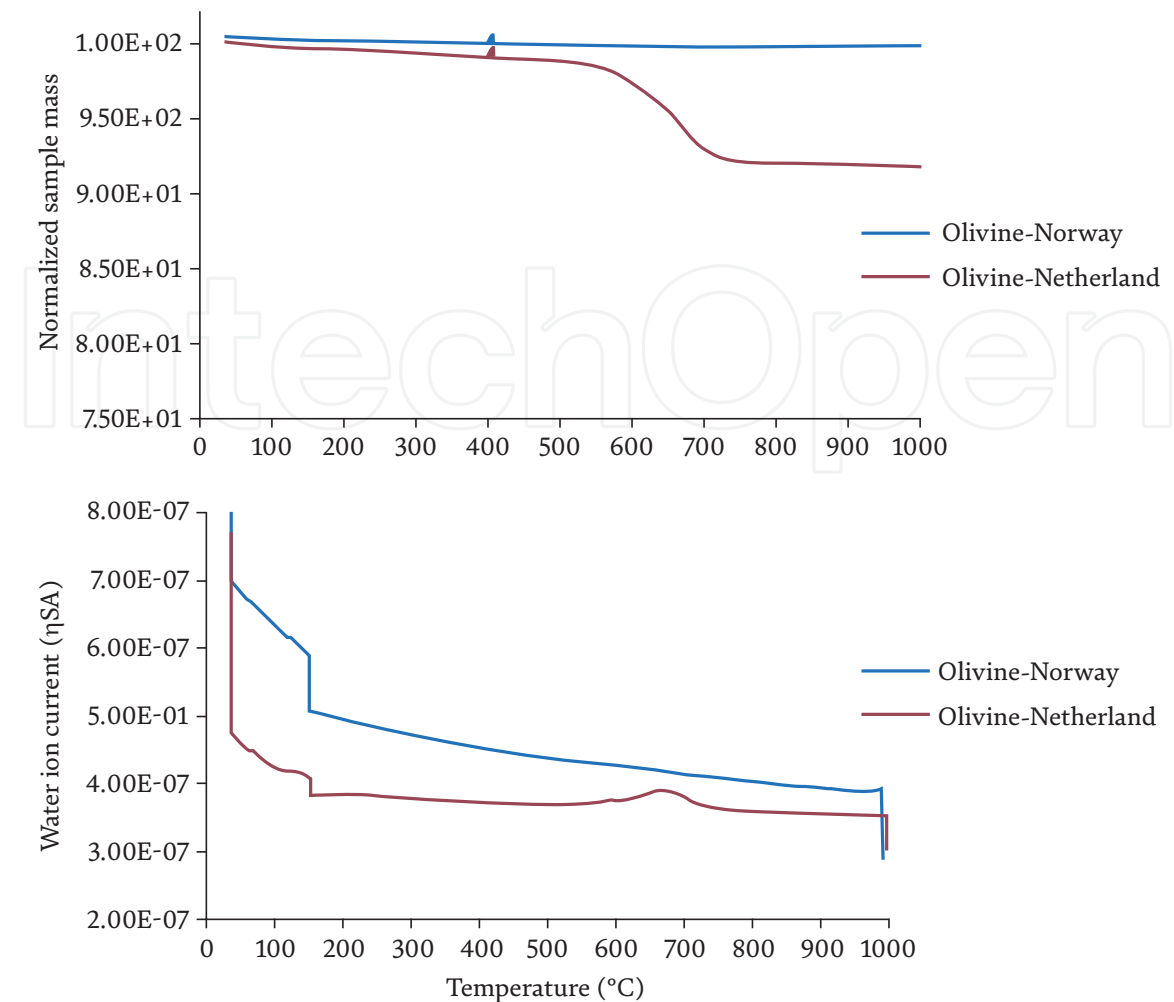
Figure 14.
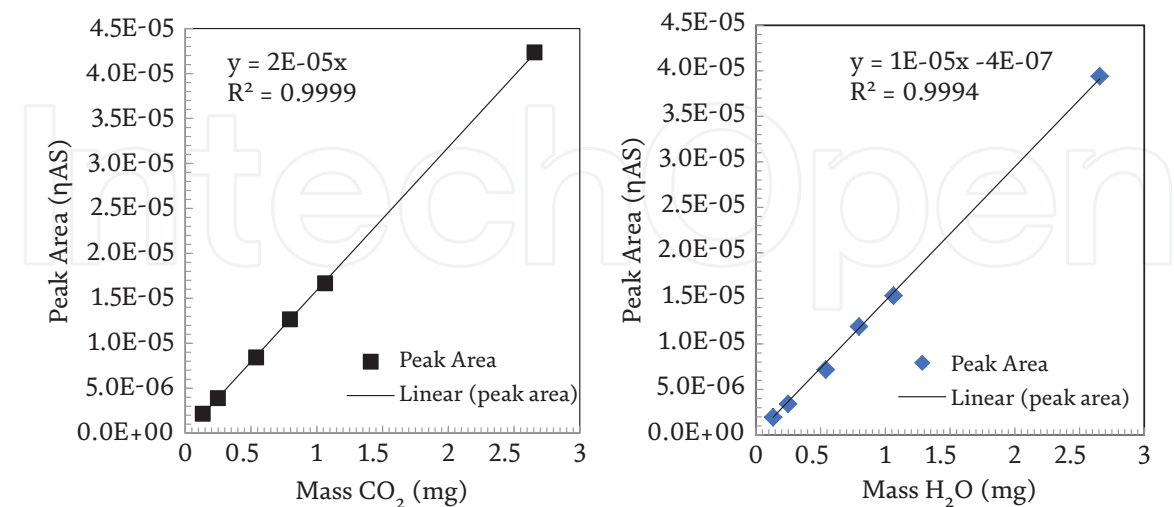*TGA-MS analysis of olivine (Norway) and olivine (Netherland).*

Figure 15.
Calibration curve to calculate mass loss of CO_2 (left), Calibration curve to calibrate mass loss of H_2O (right).

These results at least partially confirm that Olivine (Netherland) has more lizardite and is 53.01% as shown in **Table 4**. This verifies QXRD analysis. Dunite for this research was handpicked from Doonba deposit in vicinity of a small village/town Barbara, close to Tamworth city. **Tables 5** and **6** and other following tables present

	Lizardite	Olivine	Brucite	Magnetite
20–45 μm dunite	70	28	1.2	0.23
20–45 μm dunite	69	29	1.9	0.43
20–45 μm dunite	71	27	1.5	0.27
20–45 μm dunite	71	27	0.82	0.25
20–45 μm dunite	72	26	1.3	0.17

Table 5.
Semiquantitative XRD results (3 times XRD repeat, 2 reanalyses).

		Lizardite	Olivine	Brucite	Magnetite
−75 μm dunite		61	29	8.3	1.3
20–45 μm dunite		51	42	5.2	1.3
20–45 μm dunite repeat		51	42	5.9	1.3
45–75 μm		50	43	6	1.3
−20 μm dunite		66	24	8.6	1.3
Sr. No		**Lizardite**	**Olivine**	**Brucite**	**Magnetite**
1	−75 μm dunite QXRD	61	32	6.4	0.37
	−75 μm dunite TGA-MS	61	30 (difference)	8.3	0.37 (XRD)

Variation of results with the variation of size, e.g., −75 μm, 20–45 μm, 45–75 μm, −20 μm is interesting.

Table 6.
TGA-MS analysis results.

phases present in this dunite. Sub 75 μm dunite have 61% lizardite, 29% olivine, 8.3% brucite and 1.3% magnetite [18]. Percentage phases for other dunite fractions (20–45-micron, 45–75 micron and sub 20 micron) are presented in **Table 6**. An example of calibration curves for TGA-MS calibration is provided in **Figure 15**, routinely calibration was performed. Dunite is used here for calibration.

4.2 Yield calculation from dunite carbonated product

For magnesite yield calculation, please refer to earlier publication [10].

Carbonated products were heated in TGA from 25 to 1000°C and mass losses due to decomposition of different phases present are identified. To identify the evolving gases generated during heating, the TGA-DSC (Setsys Evolution 1200) was coupled with a mass spectrometer (Thermostar Quadrupole). Lizardite decomposes over the same temperature range (300–600°C) as the magnesite and this can introduce a slight systematic error in magnesite yield estimation (leading to an over-estimation of the magnesite yield) unless the mass loss in this period can be quantitatively attributed to loss of H_2O or CO_2 from the sample. To distinguish between these species, the ion current from the $m/z = 44$ ion (CO_2^+) from mass spectrometer was calibrated using sodium bicarbonate samples and a calibration curve for CO_2 concentration is obtained, which is used to quantify CO_2 mass loss (distinguishing CO_2 production from the loss of water vapour which occurs simultaneously) and thus render more accurate estimation of the magnesite yield. CO_2 peak areas were calculated using the
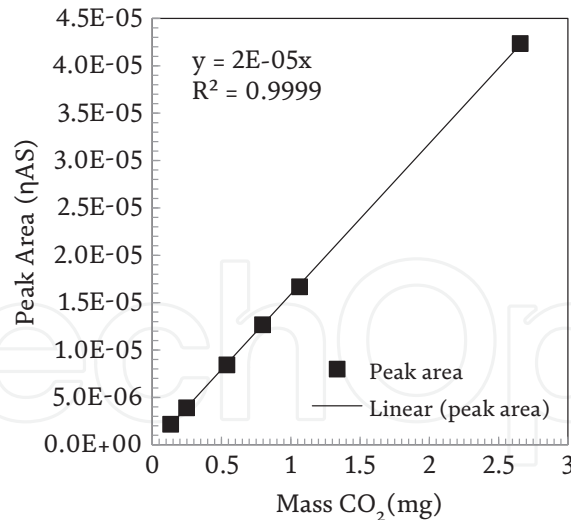
Figure 16.
Calibration curve to calculate mass loss of CO_2.

mass spectrometer data and CO_2 mass response is estimated based on the reaction ($2NaHCO_3 \rightarrow Na_2CO_3 + CO_2 + H_2O$). The relationship between peak areas and CO_2 mass loss was linear as shown in the CO_2 calibration curve (**Figure 16**).

For carbonated samples, the CO_2 peak areas were estimated using MS data and then these peak areas are used to determine CO_2 mass loss applying the CO_2 calibration curve. This CO_2 mass loss was used in Eq. (6) to calculate magnesite yield. Eq. (6) is based on the Gadikota formula (4).

Calculating fraction of magnesium (y_{Mg}) in dunite

$$\text{Yield (Rx)} = \left[\frac{\text{Measured weight ratio of } CO_2 \text{ stored in mineral}}{\text{The residual } CO_2 \text{ storage capacity}} \right] \times 100\%$$

$$= \frac{\left(\frac{W_{CO_2}}{W_{\text{mineral}}} \right)}{\frac{1}{R_{CO_2}}} \times 100\%$$

$$= R_{CO_2} \times \left(\frac{\text{TGA}}{(100 - \text{TGA})} \right) \times 100\%$$

$$= R_{CO_2} \times \left(\frac{\text{TGA}}{(100 - \text{TGA})} \right) \times 100\% \qquad (3)$$

$$CO_2 \text{ storage capacity of dunite} = \frac{1}{RCO_2} = \left(\frac{y_{Mg}}{MW_{Mg}} + \frac{y_{Ca}}{MW_{Ca}} \right) \times MW_{CO_2} \qquad (4)$$

$$\%\text{of Mg in MgO} = \left(\frac{MW_{Mg}}{MW_{MgO}} \right) \times 100\% = \left(\frac{24.3}{40.3} \right) \times 100\% = 60.3\%$$

$$\%\text{of MgO in dunite} = 42.6\%$$

$$\%\text{of Mg in dunite} = 60.3\% \times 0.426 = 25.7\%$$

$$y_{Mg} = 0.257 \text{ (using this value in equation 5)}$$

Calculating fraction of calcium (y_{Ca}) in dunite

$$\%\text{of Ca in CaO} = \left(\frac{MW_{Ca}}{MW_{Cao}} \right) \times 100\% = \left(\frac{40}{56} \right) \times 100\% = 71.4\%$$

$$\%\text{of CaO in dunite} = 0.35\%$$

$$\%\text{of Ca in dunite} = 71.4\% \times 0.0035 = 0.25\%$$

$$y_{Ca} = 0.0025 \ (\text{using this value in Eq. 5})$$

$$\frac{1}{\text{RCO}_2} = \left(\frac{y_{Mg}}{MW_{Mg}} + \frac{y_{Ca}}{MW_{Ca}}\right) \times \text{MW}_{\text{CO}_2} (equation\ 5)$$

$$\frac{1}{\text{RCO}_2} = \left(\frac{0.257}{24.3} + \frac{0.0025}{40}\right) \times 44 = 0.468$$

$$\text{RCO}_2 = \left(\frac{1}{0.468}\right) = 2.136 \ (using\ this\ value\ in\ equation\ 4)$$

$$\text{Yield (Rx)} = 2.136 \times \left(\frac{\text{TGA}}{(100 - \text{TGA})}\right) \times 100\% \qquad (5)$$

W_{CO2} = Weight of CO_2 present in dunite before carbonation.
$W_{mineral}$ = Weight of dunite present before carbonation.
$1/R_{CO_2}$ = CO_2 storage capacity of dunite.
y_{Mg} = Weight fraction of magnesium present in dunite which can react with CO_2.
MW_{Mg} = Molecular weight of magnesium (24.3 g/g mol).
MW_{MgO} = Molecular weight MgO (40.3 g/g mol).
y_{Ca} = Weight fraction of calcium present in dunite which can react with CO_2.
MW_{Ca} = Molecular weight of calcium (40 g/g mol).
MW_{CaO} = Molecular weight of CaO (56 g/g mol).
MW_{CO2} = Molecular weight of CO_2 (44 g/g mol).
R_{CO2} = Mass of dunite required to store unit mass of CO_2.
TGA = CO_2 mass loss from calibration curve.
R_X = Yield or extent of carbonation.

For a detailed description of materials, analytical instruments and experimental methods, please refer to Chapter 3 of the Ph.D. thesis [2]. Materials, Dunite, heat-activated dunite, heat-transformed dunite, twin sisters mountain dunite, olivine, lizardite and heat-activated lizardite are discussed. Analytical instruments, TGA-MS, XRD, Semi-Quantitative XRD (QXRD), ICP-OES, SEM, EDS, TEM, FTIR and Malvern Mastersizer are discussed. Experimental methods, acid dissolution, regrinding, single-stage carbonation, acrylic reactor testing without temperature and pressure, concurrent grinding both in situ and in operando and two-stage carbonation are discussed. Please refer to these publications for further details [2, 10, 13, 14, 18, 19].

A comparison of elemental composition of dunite by ICP-OES and XRF is provided in **Table 7**.

4.3 Magnesite yield results using different feedstocks

Magnesite yield results using various feedstocks are presented in **Table 8**.

Few of these results are presented graphically in **Figure 17**. For already published results, please refer to [2, 19] and [10, 18] and [13, 14]. Soaked dunite especially heat-activated provided the highest yields. This is not evident from literature, especially for heat-activated dunite. However, for raw dunite, some results are presented in Ph.D.

Element	ICP-OES (wt %)	XRF (wt %)
Mg	25.8 ± 1	25.7
Si	12.4 ± 0.3	16.6
Fe	6.38 ± 0.3	6.46
Ca	0.373 ± 0.07	0.251
K	0.04 ± 0.01	0.0015
Al	0.285 ± 0.04	0.171

This is a preliminary analysis comparison.

Table 7.
Comparison of elemental composition of dunite by ICP-OES and XRF.

Sr. No	Particle Size (μm)	Material	Reaction condition	Experiment condition	Reaction time (h)	Yield (%)
1	Sub 75	dunite	185°C, 130 bar, 15% solids, 0.64 M NaHCO$_3$	raw	1	24
2	Sub 75	dunite	185°C, 130 bar, 15% solids, 0.64 M NaHCO$_3$	Raw and regrinding	1.5	24
3	Sub 75	dunite	185°C, 130 bar, 15% solids, 0.64 M NaHCO$_3$	Heat-activated (630°C, 4 hrs)	1	37
4	Sub 75	dunite	185°C, 130 bar, 15% solids, 0.64 M NaHCO$_3$	Soaked 15 days	1	20
5	Sub 75	dunite	185°C, 130 bar, 15% solids, 0.64 M NaHCO$_3$	Soaked 30 days	1	22
6	Sub 75	dunite	185°C, 130 bar, 15% solids, 0.64 M NaHCO$_3$	raw	1	19
7	Sub 75	lizardite	185°C, 130 bar, 15% solids, 0.64 M NaHCO$_3$	raw	1	2.2
8	Sub 75	dunite	185°C, 130 bar, 15% solids, 0.64 M NaHCO$_3$	Heat-transformed (800°C, 3 hrs)	1	18
9	Sub 75	dunite	185°C, 130 bar, 15% solids, 0.64 M NaHCO$_3$	Heat-transformed (800°C, 3 hrs)	1	18
10	Sub 75	dunite	185°C, 130 bar, 15% solids, 0.64 M NaHCO$_3$	Heat-activated (630°C, 4 hrs)	1	37
11	Sub 75	dunite	185°C, 130 bar, 15% solids, 0.64 M NaHCO$_3$	Heat-activated (630°C, 4 hrs), 1 month soaked	1	42
12	20–45	dunite	180°C, 130 bar, 15% solids, 0.64 M NaHCO$_3$	Reference	2.5	5.3
13	20–45	dunite	180°C, 130 bar, 15% solids, 0.64 M NaHCO$_3$	Concurrent ground	2.5	31.6
14	20–45	dunite	180°C, 130 bar, 30% solids, 0.64 M NaHCO$_3$	Concurrent ground	2.5	16.4
15	20–45	dunite	180°C, 65 bar, 15% solids, 0.64 M NaHCO$_3$	Concurrent ground	2.5	12
16	20–45	dunite	155°C, 65 bar, 15% solids, 0.64 M NaHCO$_3$	Concurrent ground	2.5	22.5

Sr. No	Particle Size (μm)	Material	Reaction condition	Experiment condition	Reaction time (h)	Yield (%)
17	20–45	dunite	180°C, 65 bar, 30% solids, 0.64 M NaHCO$_3$	Concurrent ground	2.5	10.4
18	20–45	dunite	155°C, 130 bar, 30% solids, 0.64 M NaHCO$_3$	Concurrent ground	2.5	10.9
19	20–45	dunite	180°C, 130 bar, 15% solids, 0.64 M NaHCO$_3$	Concurrent ground	8	62
20	Sub 20	dunite	180°C, 130 bar, 15% solids, 0.64 M NaHCO$_3$	In operando grinding	2.5	23.6
21	20–45	dunite	180°C, 130 bar, 15% solids, 0.64 M NaHCO$_3$	reference	8	12.3
22	20–45	dunite	180°C, 130 bar, 15% solids, 0.64 M NaHCO$_3$	Effect of sampling	2.5	28.2
23	20–45	dunite	180°C, 130 bar, 15% solids, 0.64 M NaHCO$_3$	Effect of sampling	1	13
24	20–45	dunite	180°C, 130 bar, 15% solids, 0.64 M NaHCO$_3$	Effect of sampling	0.5	9.3
25	20–45	dunite	180°C, 130 bar, 15% solids, 0.64 M NaHCO$_3$	Effect of sampling	0.05	6.3
26	Sub 10	dunite	180°C, 130 bar, 15% solids, 0.64 M NaHCO$_3$	In operando grinding	8	54.6
27	20–45	dunite	180°C, 130 bar, 15% solids, 0.64 M NaHCO$_3$	Concurrent grinding	2.5	31.6
28	20–45	dunite	180°C, 130 bar, 15% solids, 0.64 M NaHCO$_3$	Concurrent grinding	2.5	27.2
29	20–45	olivine	180°C, 130 bar, 15% solids, 0.64 M NaHCO$_3$	reference	2.5	0.94
30	20–45	olivine	180°C, 130 bar, 15% solids, 0.64 M NaHCO$_3$	Concurrent grinding	2.5	34.1
31	Sub 75	lizardite	180°C, 130 bar, 15% solids, 0.64 M NaHCO$_3$	Concurrent grinding	2.5	5.3
32	45–75	dunite	180°C, 130 bar, 15% solids, 0.64 M NaHCO$_3$	Concurrent grinding	2.5	7.1
33	45–75	dunite	180°C, 130 bar, 15% solids, 0.64 M NaHCO$_3$	Concurrent grinding	2.5	38.2
34	Sub 75	olivine	180°C, 130 bar, 15% solids, 0.64 M NaHCO$_3$	reference	2.5	2.4
35	Sub 75	olivine	180°C, 130 bar, 15% solids, 0.64 M NaHCO$_3$	Concurrent ground	2.5	9.2

Table 8.
Yield results for different feedstocks under various experiment and reaction conditions.

thesis. Dunite yield calculation is very easy and straightforward, please refer to my Ph.D. thesis publication. Six times higher magnesite yields, or say an increase of 600% [10, 14], or almost two times higher yields in two-stage [13] were achieved using concurrent grinding. Olivine does not accept this much, but still shows some increased trend.
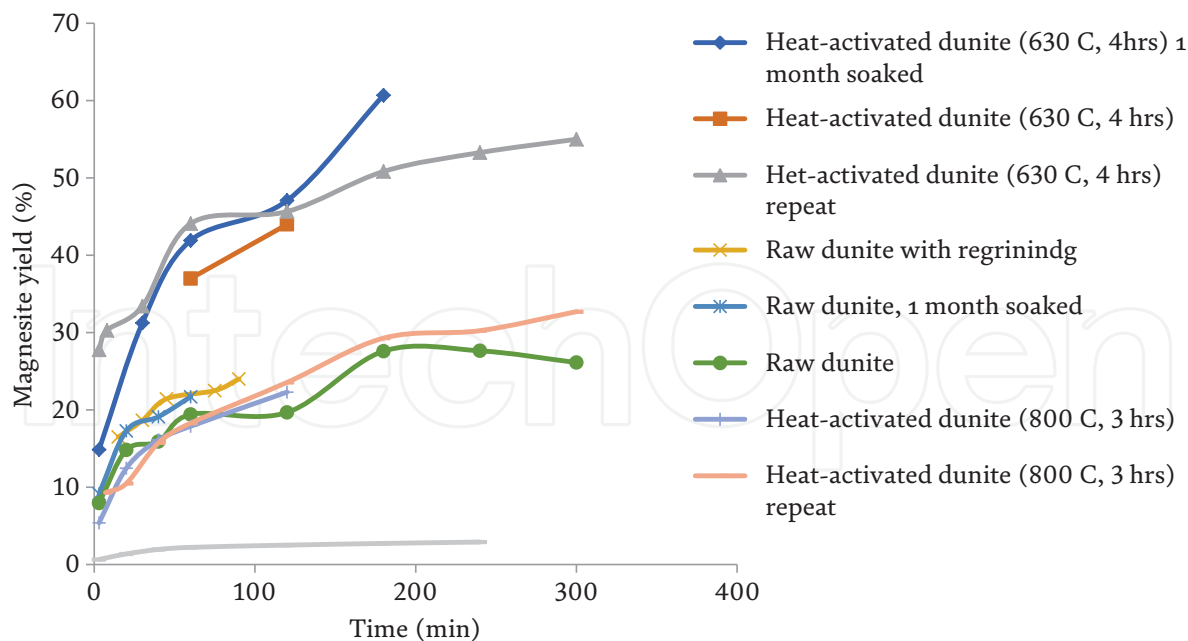
Figure 17.
Comparison of reactivity of dunite, soaked dunite, heat-activated dunite and lizardite and raw dunite soaked.

4.4 Semiquantitative XRD results authenticity

Authenticity of QXRD is shown in **Table 5**.

4.5 TGA-MS results authenticity

TGA-MS results authenticity is excellent. Please see the consistency of magnesite results, which are constant. However, these results have variations as per variation of size fraction.

Error in Brucite calculation due to slight peak overlap.
Error and second option of calculation is shown in **Figure 18**.
Sr.No. 1. QXRD Calculation details.

Csi	Cliz	Coli	Cbru	Cmag	Total
20.3	48.89	25.287	5.117	0.298	99.91
Exclude silicon	61.4	31.77	6.42	0.374	100
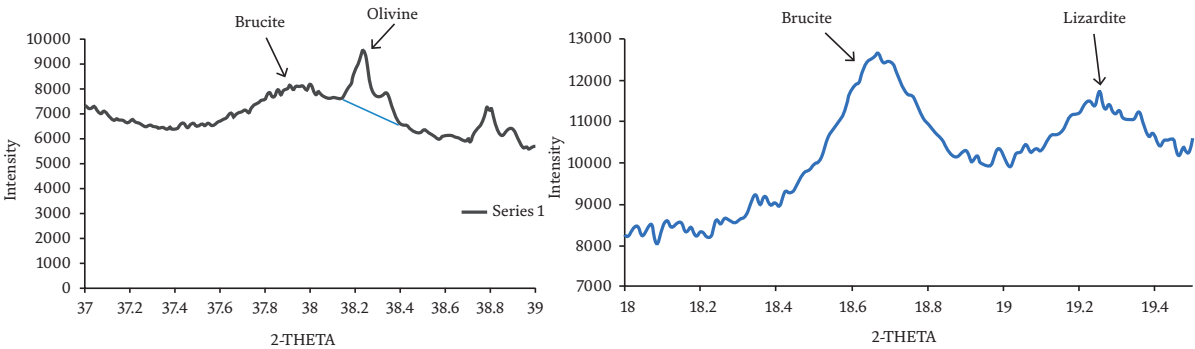
Figure 18.
The left-hand side image graph shows overlap. The right-hand side shows an alternative option.

More results related to this TGA-MS matching with QXRD.

Sr.		Lizardite	Olivine	Brucite	Magnetite
	20–45 µm dunite TGA-MS	52	42 (difference)	5.9	0.2 (XRD)
	20–45 µm dunite TGA-MS repeat	51	43.6(difference)	5.27	0.2 (XRD)
1	20–45 µm dunite QXRD	52	42	5.8	0.2
2	20–45 µm dunite QXRD repeat	52.6	42	5.27	0.19
3	20–45 µm dunite QXRD repeat	53	40	6.1	0.23

A very good match between TGA-MS and QXRD results was obtained when using an olivine peak at 17.3°. Brucite also shows a good match. The same peak points were used for all 3 XRD patterns and they are also similar to the −75 µm dunite analysis which provides more confidence in results. Points are slightly changed for 20–45 µm dunite for olivine peaks as these peaks show a slight variation. Results authenticity is excellent.

4.6 Validation of Malvern Mastersizer results

Relationship between d_{80} (mean particle size) and Malvern mastersizer RPM for olivine (**Figure 19**). The minimum RPM required for Malvern mastersizer based on feed mean size is given below.

4.7 Validation of olivine yields through QXRD measurements and matched TGA-MS

4.7.1 20: 45 µm olivine crushed carbonated sample QXRD

20–45 µm olivine crushed carbonated reference sample is mixed with 20% silicon and the sample is then scanned for semiquantitative analysis for 3 hrs. This is a reference experiment in which grinding media is not used. The reaction was done at 180°C and 130 bar. **Table 9** shows QXRD results matched with TGA-MS results.
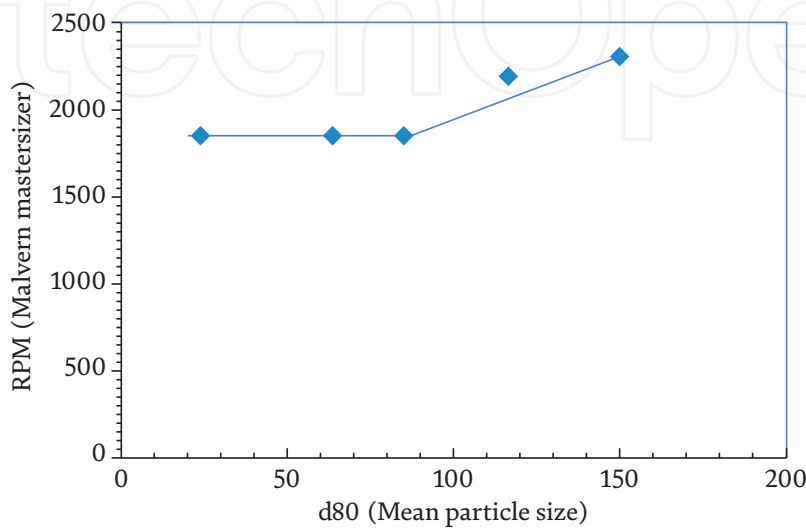

Figure 19.
Relationship between mean particle size and Malvern Mastersizer minimum RPM.

	Olivine	Lizardite	Clinochlore	Enstatite	Talc	Magnesite	Yield
20–45 μm olivine Reference Experiment	91%	0.68%	1.7%	0.36%	0.49%	5.3%	2.76%

Table 9.
QXRD analysis and yield from QXRD compared with yield from TGA-MS.

4.8 Olivine yield calculation

$$\text{Mass of } MgCO_3 = 5.3\%(\text{from QXRD}) = 0.053 \text{ g.}$$
$$= 0.053/84 = 0.000628 \text{ moles}$$

$MgCO_3 \rightarrow MgO + CO_2$.
Moles CO_2 = 0.000628 moles.
Mass CO_2 = 0.000628 * 44 = 0.02766.
Yield = (0.02766/1) * 100 = 2.76% ≥ (1%) from TGA-MS.

4.8.1 20–45 μm olivine crushed concurrent ground sample QXRD

20–45 μm olivine crushed concurrent ground sample is mixed with 20% silicon and the sample is then scanned for semiquantitative analysis for 3 hrs. This is a concurrent grinding experiment in which grinding media is used. The reaction was done at 180°C and 130 bar. **Table 10** shows QXRD results matched with TGA-MS results.

4.9 Yield calculation

$$\text{Mass of } MgCO_3 = 76\%(\text{from QXRD}) = 0.76 \text{ g.}$$
$$= 0.76/84 = 0.009 \text{ moles}$$

$MgCO_3 \rightarrow MgO + CO_2$.
Moles CO_2 = 0.009 moles.
Mass CO_2 = 0.009 * 44 = 0.396.
Yield = (0.396/1) * 100 = 39.6% ≥ (34.1%) from TGA-MS, reference [14].

4.9.1 Validation of EDS for 20–45 μm dunite resin embedded samples

Various particles analysis indicate the authenticity of EDS analysis (**Figures 20–22**). From our earlier articles, a significant difference in morphology of silica-rich layers, especially core and shell part is visible [14]. However, EDS analysis especially silicon shows no significant difference as depicted in above Figures (20–22). However,

	Olivine	Lizardite	Clinochlore	Enstatite	Talc	Magnesite	Yield
20–45 μm olivine concurrent ground experiment	19%	0.15%	0.53%	0.1%	3.6%	76%	39.6%

Table 10.
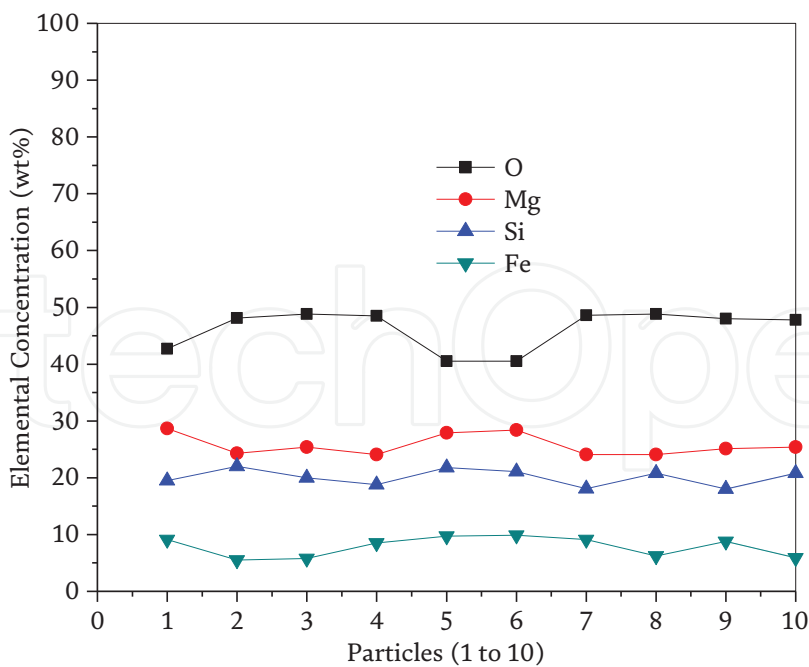*QXRD analysis and yield from QXRD compared with yield from TGA-MS.*

Figure 20.
20–45 μm dunite sample (embedded in resin) ten particles analysis.
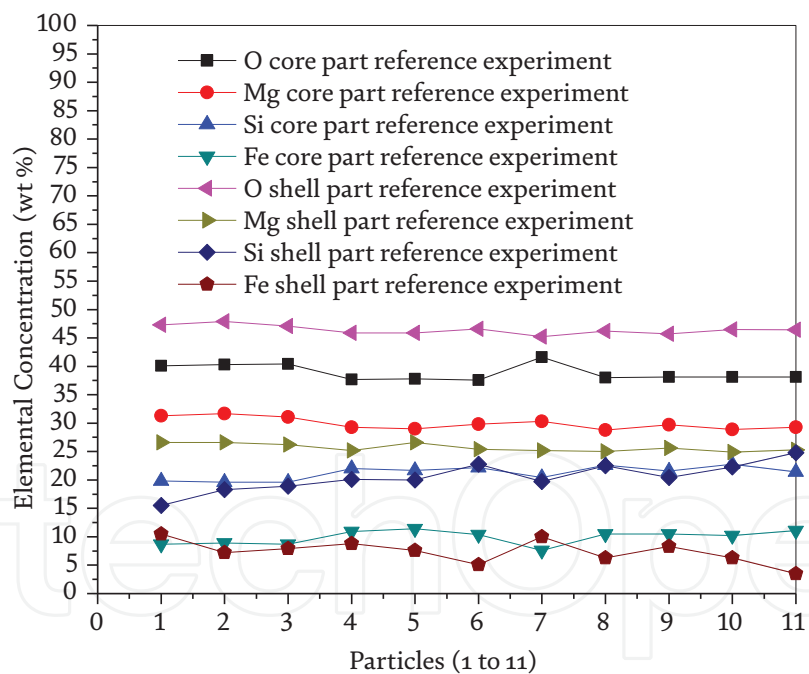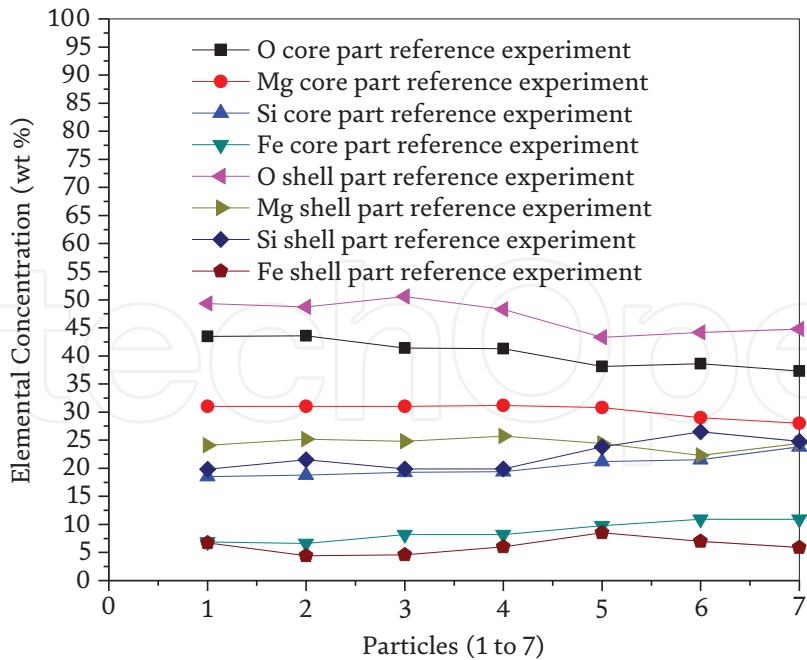

Figure 21.
20–45 μm dunite reference carbonated (8 h) sample (embedded in resin) eleven particles analysis and consistency of EDS analysis.

as reported earlier, Mg/Si ratio difference [13, 14] is there to confirm the presence of silica-rich layers. This may be taken as one of the key findings of this chapter.

5. Conclusions and recommendations

Suppliers may give wrong materials, but a variety of analyses will determine this. Semiquantitative XRD (QXRD) results authenticity is excellent. TGA-MS results

Figure 22.
20–45 μm dunite concurrent ground carbonated (8 h) sample (embedded in resin) seven particles analysis and consistency of EDS analysis.

authenticity is excellent. No doubt left on TGA-MS and QXRD results matching. ICP-OES results match with XRF results is excellent. EDS results graphically shown are excellent. Routine calibration of measuring instruments must be performed. This very instrument to instrument. Reputed researchers will know the frequency of calibration. The key to calibration is that calibration results match with standard calibration figures/charts or numbers provided by the supplier of the instrument. I recommend contacting the supplier directly or indirectly if calibration curves results are not matching as per intended results. I recommend using pure standard materials for calibration of TGA, MS, ICP-OES, XRD, SEM, EDS, TEM, Malvern Mastersizer, ATR, TPD and other measuring instruments.

Acknowledgements

Author details

Muhammad Imran Rashid[1,2]

1 Discipline of Chemical Engineering, The University of Newcastle, NSW, Australia

2 Department of Chemical, Polymer and Composite Material Engineering, University of Engineering and Technology, Lahore, Pakistan

*Address all correspondence to: muhammadimran.rashid@uon.edu.au

IntechOpen

References

[1] Tans P, Keeling R. Trends in Atmospheric Carbon Dioxide: Mauna Loa, Hawaii. Washington, DC: National Oceanic and Atmospheric Administration, U.S. Department of Commerce; 2010

[2] Rashid MI. Mineral Carbonation of CO2 using Alternative Feedstocks. Australia: The University of Newcastle; 2019

[3] Rashid MI, Benhelal E, Rafiq S. Reduction of greenhouse gas emissions from gas, oil, and coal power plants in Pakistan by carbon capture and storage (CCS): A review. Chemical Engineering & Technology. 2020;**43**(11):2140-2148

[4] Emad Benhelal JH, Zhao G, Rashid MI, Oliver T, Rayson M, Brent G, et al. Insights into chemical stability of Mg-silicates and silica in aqueous systems using 25Mg and 29Si solid-state MAS NMR spectroscopy: Applications for CO2 capture and utilisation. Chemical Engineering Journal. 2020

[5] Farhang F, Oliver TK, Rayson M, Brent G, Stockenhuber M, Kennedy E. Experimental study on the precipitation of magnesite from thermally activated serpentine for CO2 sequestration. Chemical Engineering Journal. 2016;**303** (Supplement C):439-449

[6] Julcour C, Bourgeois F, Bonfils B, Benhamed I, Guyot F, Bodénan F, et al. Development of an attrition-leaching hybrid process for direct aqueous mineral carbonation. Chemical Engineering Journal. 2015;**262**:716-726

[7] Oliver TK, Farhang F, Hodgins TW, Rayson MS, Brent GF, Molloy TS, et al. CO2 capture modeling using heat-activated serpentinite slurries. Energy & Fuels. 2019;**33**(3):1753-1766

[8] Benhelal E, Oliver TK, Farhang F, Hook JM, Rayson MS, Brent GF, et al. Structure of silica polymers and reaction mechanism for formation of silica-rich precipitated phases in direct aqueous carbon mineralization. Industrial & Engineering Chemistry Research. 2020;**59**(15):6828-6839

[9] Benhelal E, Rashid MI, Holt C, Rayson MS, Brent G, Hook JM, et al. The utilisation of feed and byproducts of mineral carbonation processes as pozzolanic cement replacements. Journal of Cleaner Production. 2018;**186**:499-513

[10] Rashid MI, Benhelal E, Farhang F, Oliver TK, Rayson MS, Brent GF, et al. Development of concurrent grinding for application in aqueous mineral carbonation. Journal of Cleaner Production. 2019;**212**:151-161

[11] Benhelal E, Rashid MI, Rayson MS, Prigge J-D, Molloy S, Brent GF, et al. Study on mineral carbonation of heat activated lizardite at pilot and laboratory scale. Journal of CO2 Utilization. 2018;**26**: 230-238

[12] Farhang F, Oliver TK, Rayson MS, Brent GF, Molloy TS, Stockenhuber M, et al. Dissolution of heat activated serpentine for CO2 sequestration: The effect of silica precipitation at different temperature and pH values. Journal of CO2 Utilization. 2019;**30**:123-129

[13] Rashid MI, Benhelal E, Farhang F, Oliver TK, Stockenhuber M, Kennedy EM. Application of a concurrent grinding technique for two-stage aqueous mineral carbonation. Journal of CO2 Utilization. 2020;**42**:101347

[14] Rashid MI, Benhelal E, Farhang F, Oliver TK, Stockenhuber M, Kennedy EM. Application of concurrent

grinding in direct aqueous carbonation of magnesium silicates. Journal of CO2 Utilization. 2021;**48**:101516

[15] Oliver TK, Dlugogorski BZ, Kennedy EM. Biologically enhanced degassing and precipitation of magnesium carbonates derived from bicarbonate solutions. Minerals Engineering. 2014;**61**(0):113-120

[16] Rashid NRMI. Fluid mechanics and heat-transfer operations combination involved in urea unit of fertilizer complex. Non-Metallic Material Science. 2019;**1**(1):5-10

[17] Muhammad NR, Rashid I. Urea Synthesis Hazard Analysis—PHA, HAZOP and Quantitative Risk Assessment, LAMBERT Academic Publishing AG & Co. KG. Germany; 2012

[18] Rashid MI, Benhelal E, Farhang F, Oliver TK, Rayson MS, Brent GF, et al. ACEME: Direct aqueous mineral carbonation of dunite rock. Environmental Progress & Sustainable Energy. 2019;**38**(3):e13075

[19] Rashid MI, Benhelal E, Farhang F, Stockenhuber M, Kennedy EM. Magnesium leachability of Mg-silicate peridotites: The effect on magnesite yield of a mineral carbonation process. Minerals. 2020;**10**:1091

[20] Benhelal E, Rashid MI, Rayson MS, Oliver TK, Brent G, Stockenhuber M, et al. "ACEME": Synthesis and characterization of reactive silica residues from two stage mineral carbonation Process. Environmental Progress & Sustainable Energy. 2019;**38**(3):e13066

[21] Shaffer G. Long-term effectiveness and consequences of carbon dioxide sequestration. Nature Geoscience. 2010; **3**(7):464-467

[22] Peters A. This startup is using sunlight and capture CO2 to make jet fuel. In: Read M, editor. Dimensional Energy. 2021

[23] Fischer EM, Sippel S, Knutti R. Increasing probability of record-shattering climate extremes. Nature Climate Change. 2021;**11**(8):689-695

[24] Ju L, Tan X, Mao X, Gu Y, Smith S, Du A, et al. Controllable CO2 electrocatalytic reduction via ferroelectric switching on single atom anchored In2Se3 monolayer. Nature Communications. 2021;**12**(1):5128

[25] Vaughan A. We are Nowhere Near Keeping Warming Below 1.5°C Despite Climate Plans Availbale from: https://www.newscientist.com/article/2269432-we-are-nowhere-near-keeping-warming-below-1-5c-despite-climate-plans/#ixzz78ZUV14CM. NewScientist; 2021

[26] Benhelal E, Shamsaei E, Rashid MI. Novel modifications in a conventional clinker making process for sustainable cement production. Journal of Cleaner Production. 2019;**221**:389-397

[27] Naseem S, Rashid MI, Ramzan N. Coal as an energy source for mitigating energy crisis in Pakistan. Journal of Engineering and Technology. 2014;**4**(2): 127-134

[28] Gadikota G, Matter J, Kelemen P, Park AHA. Chemical and morphological changes during olivine carbonation for CO2 storage in the presence of NaCl and NaHCO3. Physical Chemistry Chemical Physics. 2014;**16**(10):4679-4693

[29] Balucan RD. Thermal Studies of Magnesium Silicates from The Great Serpentine Belt in New South Wales for CO2 Sequestration by Mineral

Carbonation in. Australia The University of Newcastle; 2012

[30] Treacy M, Higgins J. Powder Pattern Simulations of Disordered Intergrowths, in Collection of Simulated XRD Powder Patterns for Zeolites. fifth ed. Amsterdam: Elsevier Science B.V.; 2007. pp. 477-485

[31] Cullity BD, Stock SR. Elements of X-ray Diffraction. Prentice Hall; 2001

[32] Lavina B, Dera P, Downs RT. Modern X-ray diffraction methods in mineralogy and geosciences. Reviews in Mineralogy and Geochemistry. 2014;**78**:1-31

[33] Rezaaiyaan GMHR, Anderson H, Kaiser H, Meddings B. Design and construction of a low-flow, low-power torch for inductively coupled plasma spectrometry. Applied Spectroscopy. 1982;**36**(6):627-631

[34] Huang M, Hieftje GM. Simultaneous measurement of spatially resolved electron temperatures, electron number densities and gas temperatures by laser light scattering from the ICP. Spectrochimica Acta Part B: Atomic Spectroscopy. 1989;**44**(8):739-749

[35] Mehta R. Interactions, imaging and spectra in SEM. In: Kazmiruk V, editor. Scanning Electron Microscopy. InTech; 2012

[36] Malvern Mastersizer 2000 Manual, 2007